Diffraction-based Approaches to the In-situ Measurement of Dimensional Variations in Components Produced by Thermoplastic Micro- and Nano-embossing

Hayden K. Taylor and Duane S. Boning

Microsystems Technology Laboratories, Massachusetts Institute of Technology,
77 Massachusetts Avenue, Cambridge, MA. 02139. USA.
e-mail: hkt@mit.edu

Abstract—**We discuss the potential merits of using the diffraction of light to detect dimensional variations of micro- and nano-fluidic components embossed in transparent thermoplastic polymers. We describe one particular scheme for measuring the depths of an array of approximately micron-depth, parallel embossed channels. The component to be measured is placed in contact with a row of nine phase-relief holograms, the combination of part and holograms is transmissively illuminated, and the far-field diffraction patterns are interpreted. The scheme is designed to provide a depth resolution of ~200 nm without needing to know the intensity response of the sensor capturing the diffraction pattern, but linear or angular misalignments of the grating with the hologram of only a few microns or a few 10^{-3} rad can destroy the scheme's effectiveness.**

I. INTRODUCTION

A. Background — hot-embossing

The hot-embossing of thermoplastic polymers is considered an attractive means of manufacturing micro- and nano-fluidic devices. In hot-embossing, the thermoplastic substrate to be patterned is usually first heated above its glass-transition temperature, causing it to soften, and a rigid patterned stamp is then pressed into the polymer before both are cooled and the stamp is removed. Thermoplastic sheets are attractive as substrates for high-volume micro- and nano-fluidic applications because of their low areal cost compared to silicon or quartz, because they are often transparent — allowing optical inspection of the fluidic samples that are to be manipulated in the devices — and because they can be processed at whatever substrate size is most cost-effective — ranging from pieces smaller than a silicon wafer to continuous reels, several metres in width. The patterns of fluidic channels produced by embossing may subsequently be encapsulated beneath a second polymeric sheet.

The topographies produced by thermoplastic embossing are susceptible to certain defects, some of which are illustrated in Figure 1. In some cases the occurrence of these defects may be guarded against by occasionally removing samples from the production line and checking that those sampled parts meet their specifications. In other cases, however, defects might be known to occur in a small but substantial proportion of the parts produced, requiring each and every part to be checked so that the defective ones can be rejected. Alternatively, frequent measurements of embossed parts might be needed as part of a feedback loop controlling key parameters such as embossing temperature or pressure.

B. Detection system requirements

State-of-the-art thermal imprint systems can process approximately one silicon wafer-sized polymeric susbstrate per minute [1], and each such substrate might be expected to contain ten or more components. With continuous-roll imprinting, the rate of component production could be yet higher. In a production-scale embossing system, therefore, we envisage tens of parts per minute needing to be checked for signs of processing defects. Such requirements seem likely to preclude measurement systems requiring contact with the part or alignment at the micron-scale in any axis. Certainly any measurement procedure used needs to be non-destructive. If the success of channel encapsulation is to be checked (Figure 1a, 1b), the measurement technique also needs to be able to monitor 'buried' topographies; fortunately, the polymeric materials used are usually optically transparent. Table I summarises some objectives for an embossing metrology system that seem reasonable to the authors.

TABLE I
SUGGESTED SPECIFICATIONS FOR A THERMOPLASTIC EMBOSSING
PROCESS MONITORING SYSTEM

Property	Suggested target, and reason
Non-contact; non-destructive	No part of the measurement system should come within 1 mm of the component under test: scratching of the component and slowing of the production line need to be avoided.
Alignment-'free'	Alignment of component with measurement system should not need to be better than ±1 mm or ±1°.
Costs of system	Perhaps ~US$5k to make the system feasible to incorporate into commercial imprint systems costing ~US$100k. Should not require extensive training to use. Minimise maintenance costs.
Speed of measurement	Tens of components per minute.
Capabilities; spatial resolution of measurement	It would probably be acceptable for dedicated test structures to be included in the embossed pattern, and for them to be considered representative of the functional embossed patterns nearby on the substrate. In microfluidic systems the depths and widths of features are likely to range between 5 and 500 μm with a need to detect variations on the order of 1–10 μm; in nanofluidic systems, channels might be as shallow as ~20 nm with a need to detect variations of ~5 nm or perhaps less. It is reasonable to assume that the embossed substrates are optically transparent down to ~300 nm.

(a) nano-channel depth variation

(b) nano-channel collapsing

(c) incomplete stamp filling

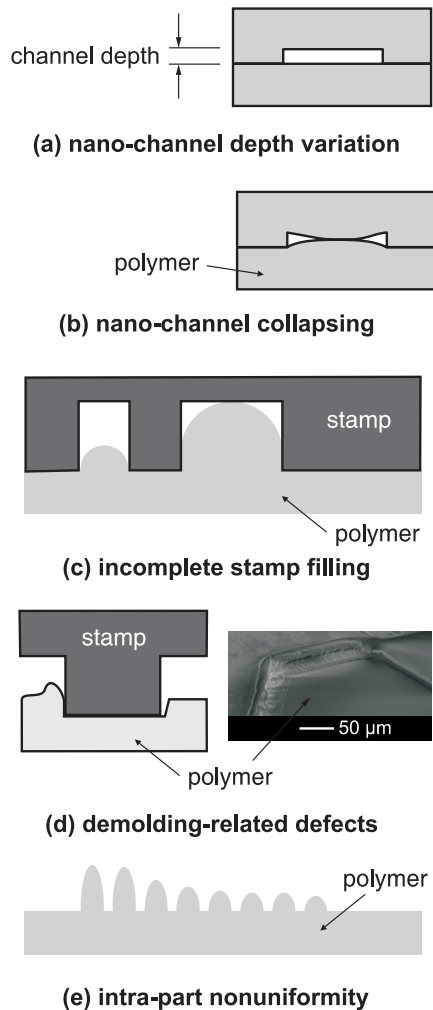**(d) demolding-related defects**

(e) intra-part nonuniformity

Fig.1. Examples of processing defects commonly encountered in hot-embossed micro- and nano-fluidic components. (a) The depths of fluidic channels may be critical to device performance (particularly in the case of sub-micron-depth channels) and may vary across and between parts. (b) Channels that are very wide in comparison with their depths may collapse during encapsulation, depending on the pressure and temperature used to bond the two polymer layers together and the surface properties of the layers. (c) Narrower features tend to form less readily than wider ones if the polymeric substrate's behaviour is rubbery when embossed. If the embossing temperature, pressure and loading duration are inadequate, stamp filling will be incomplete and nonuniform [2]. (d) Large substrates cooled in contact with the embossing stamp are liable to develop parasitic smeared edges and ridges on one side of each feature, as the polymer contracts more rapidly than the stamp [3]. (e) Embossing machine imperfections can lead to wedge-shaped pressure distributions across components, causing supposedly identical features to be formed differently.

C. Possible approaches to detection

Several established metrology techniques have been considered for the measurement of hot-embossed components [4]. For example, scanning-probe methods, including stylus profilometry and atomic force microscopy, offer the required resolutions, as does scanning white-light interferometry, but these methods probably require the part to be removed from the production line and held stationary for at least a minute. They may also require large substrates to be cut before they are measured, and these methods cannot usually measure encapsulated features — although scanning white-light interferometry can determine the topography beneath a homogeneous transparent layer of a known thickness and refractive index [5].

More attractive solutions might be found by exploiting the diffractive behavior of periodic embossed patterns. A collimated beam of monochromatic light could be directed at the component under test and the far-field diffraction pattern probed for signs of embossing defects. Because the incident radiation would be collimated, the need for contact and accurate alignment between the sensing apparatus and the part could be avoided.

In microelectronics processing, a proven non-destructive measurement technique, scatterometry, relies on interpreting the diffractive behavior of sub-micron periodic photoresist patterns [6, 7]. This technique still requires removal of the wafer from the production line: at typical feature pitches, it is necessary to sweep either the radiation's wavelength or its angle of incidence in order to obtain the necessary information about the structure. At the scales of interest for micro- and nano-fluidic systems, however, it may be possible to make simpler systems. Indeed, diffraction by an array of parallel microfluidic channels has already been demonstrated as a way of sensing the refractive index of fluid in those channels [8], and diffraction of light has been used to monitor a nanoimprint process in real-time [9]. Diffraction might similarly be used to identify processing defects.
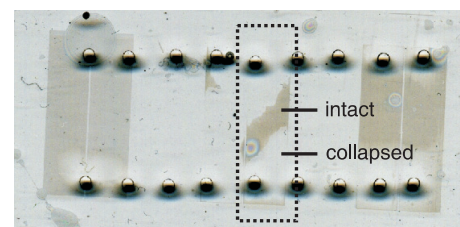
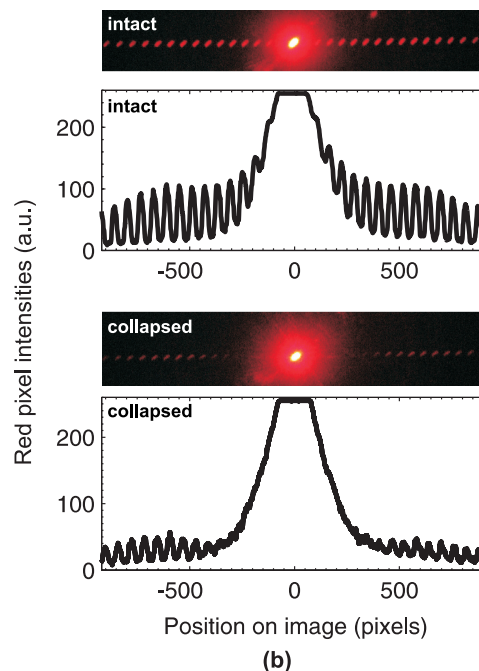**(a)** channels: height = 100 nm
width = 50 μm

(b)

Fig. 2. Identifying the collapsing of nanochannels using far-field diffraction patterns. A 632 nm-wavelength collimated laser beam was shone through an array of parallel, 50 μm-wide, 100 nm-deep embossed channels in 1.5 mm-thick PMMA, which had been encapsulated beneath a second 1.5 mm-thick PMMA sheet using oxygen plasma-activated bonding. (a) Photographic image of the sample; the dotted box indicates the region in which the channels ran. The dark patches correspond to regions of intact channels and the light regions to collapsed channels. The dark spots are holes drilled in the sample. (b) Comparison of the diffraction patterns produced by shining the laser through a patch of intact (top) and collapsed (bottom) channels.

D. Exploiting diffraction to measure embossed parts

For the time being, we are considering embossed patterns whose dimensions in the illuminated plane are many wavelengths in size, while out-of-plane dimensions may be either sub- or super-wavelength. A transparent polymeric component embossed with a periodic microscopic topography and illuminated with monochromatic, collimated light spatially modulates the phase of the transmitted light such that a Fraunhofer diffraction pattern is formed far from the component. If the embossed pattern is a regular, one-dimensional grating, the diffraction pattern formed is an array of intensity peaks whose spacing is governed by the pitch of the grating and whose relative intensities are determined by the topographical shape of each period of the grating [10]. Our work aims to identify shape variations in embossed topographies using the observed intensity distributions of far-field diffraction patterns. With this technique we aim to provide a quick, non-destructive way of identifying processing defects.

Figure 2 shows that an array of parallel, encapsulated, air-filled nanofluidic channels with depths of ~ 100 nm and a pitch of ~ 50 μm produces a Fraunhofer diffraction pattern that is distinctly suppressed when the channels collapse: when collapsing occurs, spatial modulation of the phase of transmitted light is greatly reduced. Simple gratings such as these could be useful when the number of possible processing outcomes is very limited (*e.g.* the channels either collapse, or they do not), but if quantitative information about the topography is needed (*e.g.* average channel depth in the absence of collapsing), simple gratings may not provide the best solution. For example, Figure 2 shows that the imperfectly collimated beam used to illuminate the sample has encroached on the first few diffraction orders. Collimating the beam sufficiently well to avoid that problem may be costly. Moreover, the intensity response of the image sensor would need to be calibrated in order to gather quantitative information from the diffraction pattern; even if that calibration were affordable, any spurious light falling on the sensor could invalidate measurements.

We are therefore investigating the potential of dedicated, two-dimensional holographic embossed test structures to form far-field diffraction patterns that accentuate specific embossing defects. The intention is to reduce the interpretation of diffraction patterns to a series of binary intensity comparisons, which could, if necessary, be performed with the naked eye.
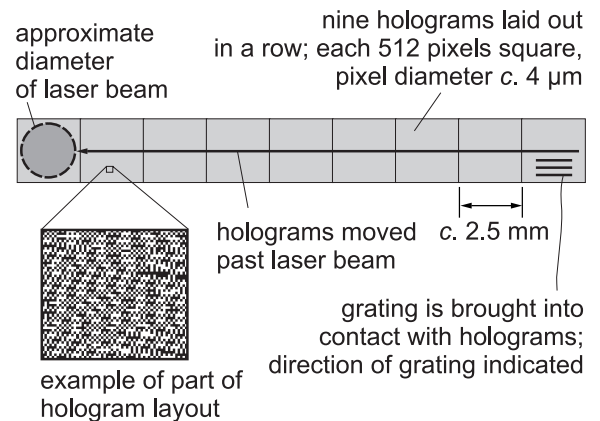
E. The proposed test pattern

One particular aim is to enable simple sub-wavelength-resolution measurement of the depths of embossed nanofluidic channels. To this end, we propose a series of nine specially designed, precisely fabricated, transparent phase-relief holograms that would be brought close to and aligned with an array of the channels to be tested. Viewing the superposition of the nine resulting far-field diffraction patterns would provide a human operator with intuitive information about the phase-relief of the channels under test, with a resolution of $\pi/4$ radians. The scheme is illustrated in Figure 3.

II. HOLOGRAM DESIGN PROCEDURE

In the proposed scheme, each of the nine 2-D reference holograms $h_k[s, t]$ has $S \times S$ pixels ($S = 512$ in this implementation) and each pixel takes one of two possible topographical levels. The holograms are assumed not to attenuate light but instead spatially to modulate its phase. The relief of the holograms is ideally (but not crucially) $\lambda_0/2(n - n_0)$, where n_0 is the refractive index of the medium surrounding the hologram (usually air), n is the refractive index of the hologram material (assumed homogenous), and λ_0 is the wavelength of the illuminating light in free space. This ideal topographical relief would allow the hologram to modulate the transmitted phase by π radians.
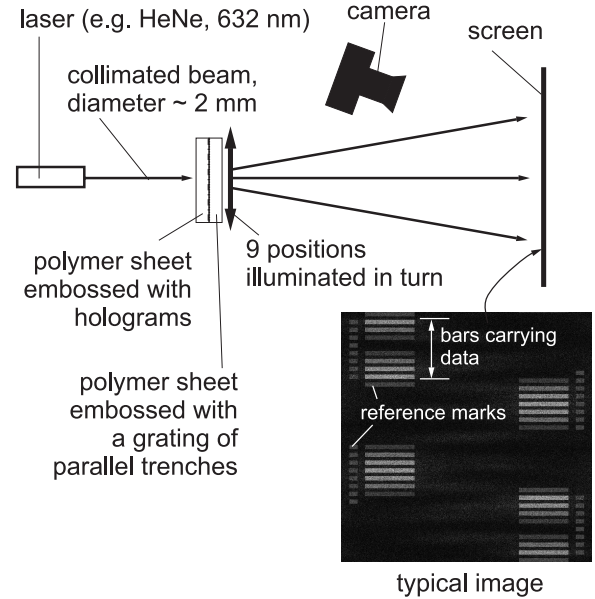
(a) test setup

(b) hologram pattern layout

Fig. 3. Channel-depth measurement scheme. (a) shows the proposed test setup, with a helium-neon 632 nm-wavelength laser having a spot diameter of ~ 2 mm, the hologram-channel array combination in the beam's path, and a screen and digital camera to capture the far-field diffraction patterns. A simulation of a typical far-field image is shown. (b) shows how the composite image is assembled: by stepping the holograms past the laser beam and capturing one image per hologram. In a production setting, each hologram might have its own illumination source or the illumination might encompass all holograms at once. In the hologram layout example, shaded pixels represent depressed regions of the transparent hologram.

Meanwhile, the width and spacing of the parallel channels to be measured are equal to the pixel diameter, $\varDelta$, of the holograms. The phase modulation depth, $\Delta\varphi$,

provided by the channel array is equal to $2\pi(n-n_0)\Delta z/\lambda_0$, where Δz is the channel depth. When the channels are placed directly in contact with the face of the holograms, running parallel to their t-axis, a discrete representation $H_k[u, v] = H_k(u\lambda_0/S\Delta, v\lambda_0/S\Delta)$ of the far-field diffraction pattern, ignoring pixel-shape effects, is given by

$$H_k[u,v] = \frac{1}{S^2}\sum_{s=1}^{S}\sum_{t=1}^{\frac{S}{2}}\left[h[2s,t]\exp\left(j\Delta\varphi\right)+h[2s-1,t]\exp\left(\frac{2\pi ju}{S}\right)\right]$$
$$\times\exp\left(-\frac{2\pi j(sv+2tu)}{S}\right).$$

When $\Delta\varphi = \pi$, the replay field is a shifted version of that for $\Delta\varphi = 0$:

$$H[u,v]\Big|_{\Delta\varphi=\pi} = H[u-\frac{S}{2},v]\Big|_{\Delta\varphi=0}.$$

For intermediate values of $\Delta\varphi$, the diffraction pattern is a weighted superposition of the shifted and unshifted diffraction patterns, so that by comparing the relative intensities of the shifted and unshifted components we can gain an impression of the channel depth. Figure 3a illustrates a possible test setup: the hologram–channel combination is stepped across the laser beam, and the camera captures one image per hologram. These images are then merged to build an image such as that illustrated in the figure.

The holograms are designed (after [11]) as follows. We begin with a matrix describing the target intensity distribution of the far-field diffraction pattern: each element of the matrix is set to either 1 or 0. A phase mask is then created, with each element of the mask taking a randomly chosen value that is uniformly distributed between 0 and 2π. The target intensity pattern and the phase mask are then used to build a matrix containing complex far-field target amplitudes. The inverse Fourier transform of this complex matrix is taken, yielding an ideal transmission function for the hologram. The amplitude information in this transmission function is discarded because the holograms in this implementation are transparent. The phase information in the transmission function is then quantized to values of either 0 or π, so that the hologram can be fabricated with only two levels of relief. The imposition of the random phase mask on the target image is thought to reduce, although not to optimize, quantization noise.

The first hologram of the nine, h_1, is designed to produce a set of eight 'tick marks' in the first and third quadrants of the far-field (u, v) plane. Each of the remaining holograms is designed to produce a far-field image of a rectangular bar aligned with a different one of the tick marks in the first and third quadrants of the (u, v) plane. Each hologram $h_{k=2-9}$ is synthesised so that its rectangular bar appears at its brightest in the first and third quadrants of the (u, v) plane when a specific value, $\Delta\varphi_k = (k-1)(\pi/4)$, is taken by the phase-relief of the grating under test. This design objective is achieved by adding a step into the hologram synthesis procedure whereby, prior to quantization, we decrease by $\Delta\varphi_k$ the phase of elements of the ideal transmission function having even s indices.

The far-field diffraction patterns from all nine holograms, when combined, produce a set of rectangular bars with differing brightnesses; the locations of the brightest and dimmest bars can then be used to deduce to

the phase-relief $\Delta\varphi$ of the grating under test, as shown in Figure 4.

The maximum phase-relief resolution of the system is equal to 2π radians divided by the number of bars in the combined far-field image: in the present implementation, with eight bars, the maximum resolution is $\pi/4$ radians. The scheme enables unambiguous measurement of channel depths less than $\lambda_0/(n-n_0)$, which is approximately 1.5 µm for red light and the polymer poly(methyl-methacrylate) (PMMA).

However, a one-pixel transverse offset of the grating relative to the hologram is equivalent to a sign change of the phase-relief as defined in Figure 4, meaning that if the precise position of the grating's trenches relative to the hologram is unknown, the system is only able to distinguish unambiguously between phase-reliefs up to π radians.

Similarly, imperfect angular alignment of the holograms with the grating is equivalent to subjecting half of the area of the grating to a lateral offset of one pixel relative to the hologram. Imperfect angular alignment will therefore lead to a blurring of the diffraction image seen — unless the phase-relief of the grating is exactly π, in which case we do not expect angular or linear offsets to affect the diffraction pattern.
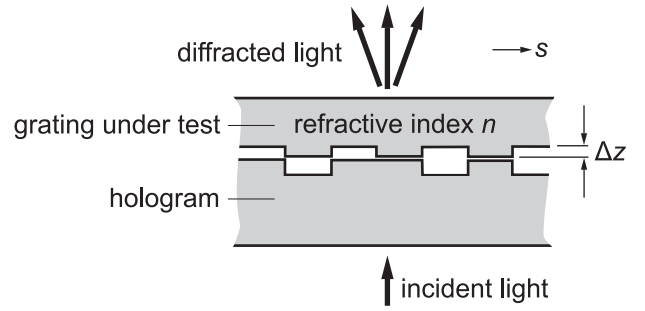
(a) test setup
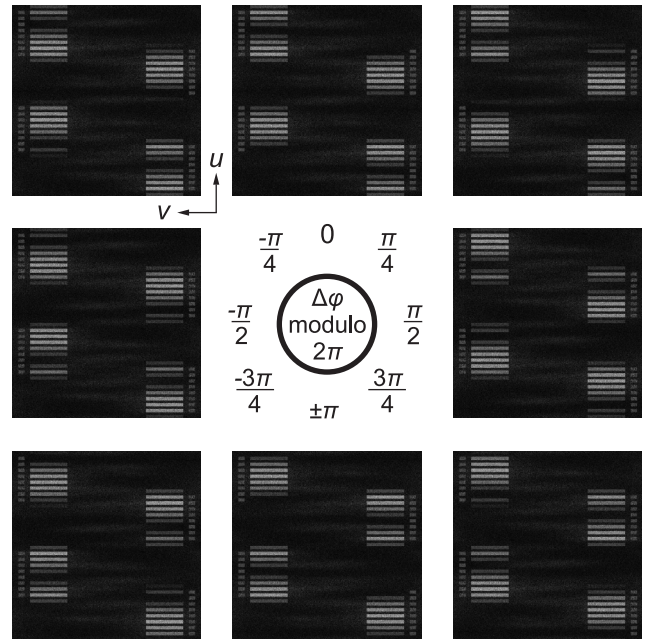
(b) simulated far-field diffraction images

Fig. 4. How the holograms are used to determine the phase-relief of the grating of channels under test. (a) Close-up of the test setup, with the grating in contact and alignment with the holograms. (b) Simulations of the evolution of composite far-field diffraction patterns as the phase-relief $\Delta\varphi$ of the channels varies.

III. TESTING METHOD

The hologram designs were arranged in a row and several separate, scaled copies were transferred to a chrome-on-glass photolithographic mask, with pixel sizes Δ ranging from 4 to 9 μm. Arrays of parallel lines with widths and spacings ranging from 4 to 9 μm were also included on the mask. A nominally 1 μm-thick layer of positive photoresist was spun on to a silicon wafer and photolithographically patterned using the mask. To enable simple prototyping, a layer of the liquid resin polydimethylsiloxane (PDMS) was cast on to the patterned resist surface and, when cured, was peeled off, producing a set of holograms and parallel channels with a nominal topographical relief of 1 μm. A second wafer was photolithographically patterned in the same way, but 120 nm of nickel was then evaporated on to the wafer and the photoresist subsequently lifted off using acetone. The resulting stamp was then embossed into a 1.5 mm-thick layer of PMMA at a temperature of 125 °C and a pressure of 2 MPa. A third wafer was patterned with the same mask and etched to a depth of ~ 20 μm using deep reactive ion etching; the resulting stamp was embossed into a second sample of PMMA at 125 °C and 2 MPa.

The PDMS holograms were brought into contact, in turn, with (i) the PDMS channels with a relief of ~1 μm, (ii) the PMMA channels with a relief of ~120 nm, and (iii) the PMMA channels with a relief of several microns. Diffraction images were captured for each hologram-grating combination as indicated in Figure 3.

IV. RESULTS AND DISCUSSION

The composite images captured during the tests are shown in Figure 5. In Fig. 5a we see the image obtained with only the PDMS holograms in the optical path. The location of the dimmest of the eight bars correctly corresponds to that predicted by simulation for a grating phase-relief of zero (Figure 4b). Fig. 5b shows the diffraction pattern arising when the PDMS grating with a relief of 0.80±0.02 μm is brought into contact with the holograms. Assuming a refractive index of 1.45±0.02 for PDMS, the phase-relief of this grating is between 3.4 and 3.7 radians: *i.e.* approximately π radians. Indeed, the captured image does have its dimmest bars in the positions predicted by simulation for a phase-relief of π radians.

Fig. 5c shows the diffraction pattern obtained using the PMMA grating with a measured relief of 130±10 nm. Assuming a refractive index of 1.45±0.02 for PMMA, the phase-relief this grating is between 0.51 and 0.65 radians: *i.e.* approximately π/6 to π/5 radians. The phase-relief of this shallow grating is therefore smaller than the designed π/4-radian resolution of the system, and the location of the minimum-intensity bars in the image has not moved appreciably from the no-grating case.

The largest grating relief used was measured as 2.3±0.1 μm (Fig. 5d) and here the experimental diffraction patterns show all bars having a relatively uniform intensity. It is believed that because the ridges of this grating have a tapered cross-sectional profile, the phase-relief of the grating does not have a sharply-defined value, so that the diffraction pattern observed is in fact a combination of the patterns associated with many different phase-reliefs. In

any case, the grating used modulates the phase of the transmitted light by amounts exceeding 2π radians; even if the grating had sharp side-walls, we would be unable to determine its phase-relief unambiguously.
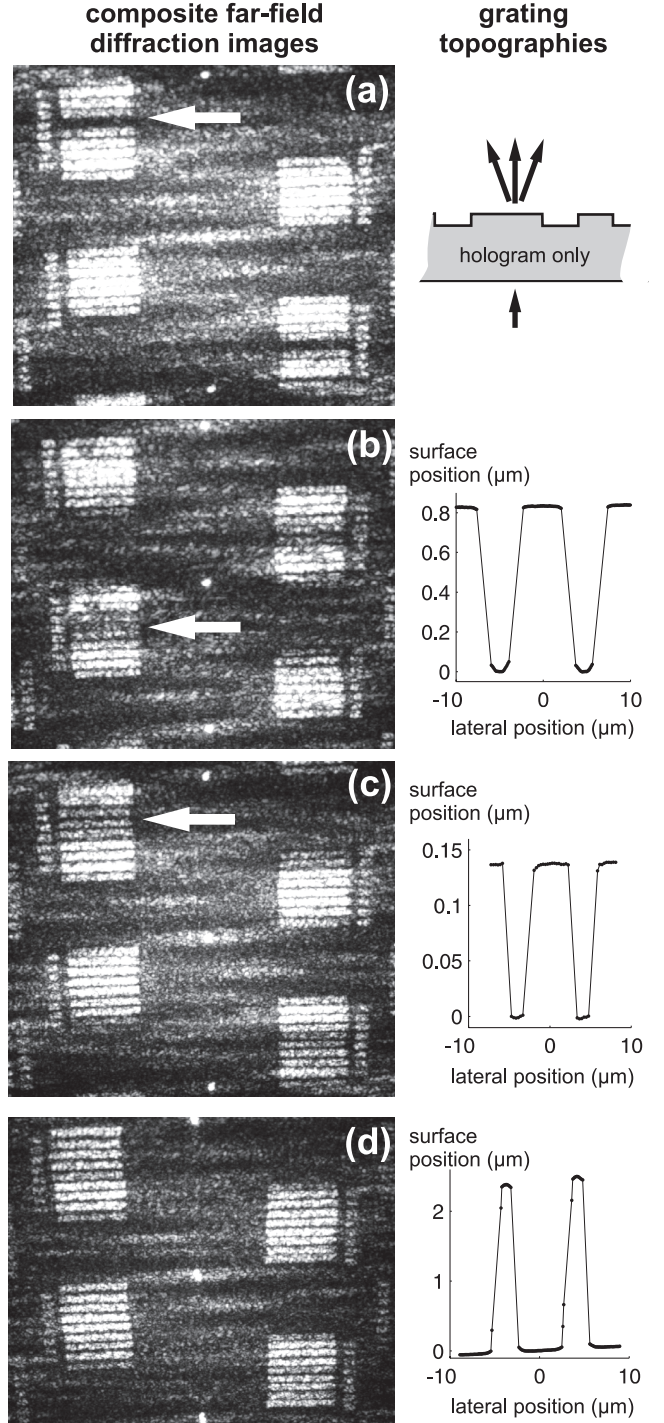

Fig. 5. Experimental results. Left: composite images of diffraction patterns obtained by shining 633 nm laser light through each of nine test holograms in turn. White arrows indicate the locations of minimum intensities. Right: topography of two ridges of each of the gratings under test, obtained with scanning white-light interferometry. (a) Diffraction pattern with holograms only; no grating; (b) with PDMS grating having a phase-relief ~π; (c) with PMMA grating having a phase-relief smaller than π/4; (d) with PMMA grating having non-sharp ridge edges and a peak relief of ~ 2 μm.

V. CONCLUSION AND OUTLOOK

The holographic measurement scheme described here has been shown to distinguish between a grating of parallel embossed channels with a phase-relief of approximately π radians, and gratings with substantially smaller or larger phase-reliefs. The method allows these gratings to be distinguished without first calibrating the intensity response of the image sensor capturing the diffraction patterns.

We have, however, seen that for grating phase-reliefs other than π radians, angular misalignment of the grating relative to the hologram — of even one pixel over the length of the hologram — is sufficient to blur the resulting diffraction patterns and prevent the actual phase-relief from being determined. Similarly, transverse offsets of the grating relative to the hologram — or grating profiles that are not sharp-walled — can be responsible for blurring of the diffraction images.

The present scheme therefore does not have the properties of being contact- and alignment-free that are desirable in an embossing metrology system. The scheme could, however, be used to check for errors in the processing of channel arrays whose target phase-relief is exactly π radians, since only when that processing target had been attained would the diffraction patterns produced be reasonably insensitive to hologram–grating misalignments. The scheme could also be used specifically as a test of the angular alignment of two layers, one patterned with the holograms and the other with a grating of parallel trenches with a phase-relief that was *not* equal to π radians.

In general, the use of diffraction is a promising route to non-contact, alignment-free defect detection in transparent embossed components. Our ongoing efforts include investigating diffractive test patterns that could be embossed directly into the part being produced, removing the need for a reference hologram and the associated alignment challenges. Diffraction-based defect detection could also be applied to transparent parts produced by the curing of liquid resins, or by injection moulding. We further believe that diffraction could be used to confirm whether micro- and nano-fluidic channels had been successfully filled with buffer solutions prior to use.

VI. ACKNOWLEDGEMENTS

VII. REFERENCES

[1] Obducat AB, "Sindre nanoimprint lithography system." Internet: http://www.obducat.com/Default.aspx?ID=489, [Nov. 30 2007].

[2] H. K. Taylor, D. S. Boning, C. Iliescu and B. Chen, "Computationally efficient modeling of pattern dependencies in the micro-embossing of thermoplastic polymers," presented at *Intl. Conf. Micro- and Nano-Engineering*, Copenhagen, 2007.

[3] M. Dirckx, H. Taylor and D. Hardt, "High-temperature de-molding for cycle time reduction in hot embossing," in *Proc. Soc. Plastics Engineers Annual Technical Conf.*, 2007, pp. 2972–2976.

[4] V. Shilpiekandula, D.J. Burns, K. Youcef-Toumi, K. El Rifai, S. Li, I. Reading, and S.F. Yoon, "Metrology of Microembossed Devices: a Review," in *Proc. Intl Micromanufacturing Conf.*, Sep. 2006, pp. 302–307.

[5] Veeco Instruments, "Through-transmissive media module." Internet: http://veeco.com/products/details_options.php?cat=1&sub=5&oid=2 06&subfam=206, [Nov. 30, 2007].

[6] C. J. Raymond, M. R. Murnane, S. L. Prins, S. Sohail, H. Naqvi, J. R. McNeil and J. W. Hosch, "Multiparameter grating metrology using optical scatterometry," *Journal of Vacuum Science & Technology B: Microelectronics Processing and Phenomena,* vol. 15, pp. 361 ff., 1997.

[7] T. A. Brunner and C. P. Ausschnitt, "Process monitor gratings," in *Proc. SPIE*, vol. 6518, 2007, pp. 651803 ff.

[8] O. J. A. Schueller, D. C. Duffy, J. A. Rogers, S. T. Brittain and G. M. Whitesides, "Reconfigurable diffraction gratings based on elastomeric microfluidic devices," *Sensors and Actuators A: Physical,* vol. 78, pp. 149–159, 1999.

[9] Z. Yu, H. Gao and S. Y. Chou, "RIMS (real-time imprint monitoring by scattering of light) study of pressure, temperature and resist effects on nanoimprint lithography," *Nanotechnology,* vol. 18, pp. 4 ff., 2007.

[10] M. Born, E. Wolf and A. B. Bhatia, *Principles of Optics: Electromagnetic Theory of Propagation, Interference and Diffraction of Light.*, 7th edition, Cambridge: 1999, pp. 952 ff.

[11] E. Buckley, A. Cable, T. Wilkinson and N. Lawrence, "Precision measurement with visual feedback using binary phase diffractive optical elements," *Opt. Lett.,* vol. 31, pp. 1053–1054, 2006.